batteries

MDPI

Article

Pom-Pom Flower-like Morphology of δ-MnO_2 with Superior Electrochemical Performances for Rechargeable Aqueous Zinc Ion Batteries

Priya Yadav [1,†], Dimas Putro [2,†], Jaekook Kim [2,*] and Alok Kumar Rai [1,*]

[1] Department of Chemistry, University of Delhi, Delhi 110007, India
[2] Department of Materials Science and Engineering, Chonnam National University, 300 Yongbong-dong, Bukgu, Gwangju 500-757, Republic of Korea
* Correspondence: jaekook@chonnam.ac.kr (J.K.); alokkumarrai1@gmail.com (A.K.R.)
† These authors contributed equally to this work.

Abstract: A rechargeable aqueous zinc-ion battery is an encouraging alternative for grid-scale energy storage applications, owing to its advantages of high safety, low cost, and environmental benignity. Since MnO_2 is found to be one of the most efficient intercalation cathode materials for ZIBs, the layered type δ-MnO_2 polymorph exhibits reversible intercalation/de-intercalation of Zn^{2+} ions with a high capacity. Unfortunately, the δ-MnO_2 cathode suffers from poor cyclability, low-rate capability, and structural degradation during charge–discharge cycles. Therefore, δ-MnO_2 with Pom-Pom Flower-like morphology have been synthesized using a facile hydrothermal method. The unique morphology of δ-MnO_2 provides a high surface area with numerous reaction sites, leading to excellent electrochemical performance. The obtained results revealed that the δ-MnO_2 electrode retained ~99% of its initial capacity even after 250 cycles, which can be ascribed to the reversible Zn^{2+} insertion/de-insertion from the current unique morphology of the layered δ-MnO_2 nanostructure. In addition, the electrochemical and structural investigation also indicates a two-step co-insertion of H^+ and Zn^{2+} ions into the interlayer of δ-MnO_2 during the discharge process. Thus, the superior electrochemical performances of the δ-MnO_2 cathode paves a way for the high capacity and a long lifespan of zinc-ion batteries.

Keywords: δ-MnO_2; morphology; cathode; aqueous zinc-ion batteries

Citation: Yadav, P.; Putro, D.; Kim, J.; Rai, A.K. Pom-Pom Flower-like Morphology of δ-MnO_2 with Superior Electrochemical Performances for Rechargeable Aqueous Zinc Ion Batteries. *Batteries* **2023**, *9*, 133. https://doi.org/10.3390/batteries9020133

Academic Editor: Chuang Yu

Received: 4 November 2022
Revised: 31 January 2023
Accepted: 11 February 2023
Published: 14 February 2023

1. Introduction

Rechargeable lithium-ion batteries (LIBs) were invented in 1994, which led to the revolution in the electronic world [1,2]. LIBs then became the leading device in portable electronics, mobiles, and electric vehicles [3]. However, the researchers have now switched their attention in exploring the alternatives of LIBs due to the scarcity of lithium and thereby, its increasing price [4]. Among all the recent battery research based on multivalent ions (such as aluminium [5,6], zinc [7–9], magnesium [10–12], etc.), the aqueous zinc-ion battery exhibits successful results towards Zn-ion intercalation/deintercalation owing to its non-toxicity, low cost, high theoretical capacity (~819 mAh g^{-1} and 5855 mAh cm^{-3}), favorable low redox potential (−0.78 V vs. SHE), and higher zinc-ion diffusion rates [13,14]. Furthermore, aqueous ZIBs do not even require an expensive inert-gas glove box for the assembly of cells as they can be integrated in air, resulting in the ease in manufacturing procedure [15,16]. On the other hand, the high stability of metallic zinc with good chemical stability in water makes Zn a favorable anode for ZIBs. Furthermore, zinc-containing solutions such as $ZnSO_4$ or $Zn(NO_3)_2$ act as electrolytes for ZIBs. However, developing an efficient cathode for aqueous ZIBs has become an attractive goal now for researchers to commercialize ZIB [4]. Recently, various cathode materials, such as vanadates [17], Prussian blue analogous [18,19], polymers, NASICON-type phases ($Na_3V_2(PO_4)_3$) [20], and

MnO_2 [21], have been investigated so far to build potential aqueous ZIBs. However, the NASICON-type structures and Prussian blue analogous offer a deplorable capacity [21,22]. Mantia et al. used copper hexacyanoferrate as a cathode with an aqueous electrolyte for zinc-ion batteries. [23] However, the material shows less capacity of only ~55 mAh g^{-1} at 100th cycle. On the other hand, Alshareef et al. reported a layered $Mg_xV_2O_5{\cdot}nH_2O$ cathode for aqueous ZIBs, which delivered a high capacity of ~264 mAh g^{-1} after 1000 cycles at 1000 mA g^{-1} [24]. However, the toxic nature of vanadium-based oxides limits their application as cathode materials for ZIBs. The major hurdle to investigate a suitable cathode material is the high electrostatic repulsion that exists between divalent zinc ions and the high-charge density of zinc ions that leads to the lethargic transport kinetics, which severely hinders the development of aqueous ZIBs [15]. Recently, MnO_2 is found to be an excellent cathode among the majority of the transition metal oxides due to its high theoretical capacity, less toxicity, rich natural abundance, low cost, and moderate potential window [4,25]. There are diverse crystal structures of MnO_2 named α, β, γ, δ, and λ, in which the first three phases (α, β, γ) exhibit 1D tunnel-like structures and the latter two (δ, λ) belong to a 2D layered structure and a 3D spinel structure, respectively [26,27]. As per the literature reports, it is found that all the polymorphs can host Zn^{2+} ions for aqueous ZIBs. However, the studies conducted so far revealed that the tunnel structure of MnO_2 shows serious phase transition during charge and discharge [28–30]. During the cycling process, the phase transition of α-MnO_2 to δ-MnO_2 and β-MnO_2 to the layer-type phase impacts the electrode structure and is believed to be the main reason for the capacity fade [26,31]. On the other hand, the layered δ polymorph of MnO_2 exhibits minimal structural change during Zn^{2+} ion insertion/extraction with a high surface area, resulting in the reduced diffusion paths for Zn^{2+} ions [27]. In addition, the layered δ-MnO_2 structure is also energetically and kinetically favorable and stable with a low proton adsorption energy, which inhibits phase transition during cycling [25,32]. Moreover, since δ-MnO_2 exhibits excellent capacity with high-rate performances, it is found to be a viable choice for high-energy density applications such as portable electronics and electrical vehicles. Furthermore, its cost-effectiveness also makes it considerable for large-scale industrial applications where cost is a concern [27,32]. Unfortunately, the MnO_2 cathodes generally suffered from low electrical conductivity, serious structural degradation, and the dissolution of Mn^{2+} ions, leading to the fast capacity decay and subservient rate capability.

Therefore, among all the numerous efforts to enhance the electrochemical performances of the MnO_2 cathode, morphological optimization continuously attempted to resolve these issues. Though the considerable signs of progress have been noticed toward the fabrication of MnO_2 polymorphs mainly using the carbon materials (such as graphene, carbon nanotubes, and N-doped carbons), the direct growth of MnO_2 cathodes on current collectors, binder-free MnO_2 cathodes, etc. remains a big challenge to synthesize a sustainable morphology-based MnO_2 cathode with excellent electrochemical performances using a low-cost synthesis method without even using any carbon source. Hence, in the present work, the synthesis of a pom-pom flower-like architecture of δ-MnO_2 by a facile hydrothermal synthesis method using $KMnO_4$ and $MnSO_4$ as additives is being reported for the first time. The obtained morphology of δ-MnO_2 exhibits a high surface area with excellent structural stability and provides a pathway for ion transport, which can improve the overall conductivity of the cathode. As expected, the pom-pom shaped flower-like morphology of δ-MnO_2 as a cathode offers excellent rate capability, high capacity, and long-term cyclability; thus, providing a new pathway for developing high-performance aqueous ZIBs.

2. Experimental

2.1. Material Synthesis

A δ-MnO_2 cathode with a pom-pom shaped flower-like morphology was successfully synthesized using the facile hydrothermal synthesis method. Initially, 10 mmol of $KMnO_4$ (Emplura, 99%, India) and 1.7 mmol of $MnSO_4.H_2O$ (Alfa Aesar, 99%, India) were dissolved

separately in 50 mL and 20 mL of deionized water (DI), respectively. Thereafter, both solutions were mixed and kept for stirring. After vigorous stirring for 30 min, the obtained homogeneous solution was transferred to a Teflon-lined stainless-steel autoclave and heated up to 150 °C for 14 h. Afterward, the resultant solid product was centrifuged and washed with DI and ethanol several times. The sample was then dried overnight at 75 °C. At last, the as-prepared sample was put for calcination at 360 °C for 2 h to obtain the pure sample of δ-MnO_2.

2.2. Material Characterisation

To check the crystallinity and single phase of the calcined sample, XRD was collected using a Shimadzu X-ray diffractometer with Cu Kα radiation (λ = 1.5406 Å, scanning angle (2θ) = 5–90°). The transmittance property was carried out by Fourier-transform-infrared spectroscopy (FT-IR) in the range of 400–4000 cm^{-1} using a Nicolet iS50 model of FT-IR. Raman spectroscopy (a Renishaw Raman microscope, 514 nm laser) was also used to study the phase composition of the calcined sample. The surface morphology, particles size, and elemental distribution in the sample were carried out by field emission-scanning electron microscopy (FE-SEM), field emission-transmission electron microscopy (FE-TEM, Philips TecnaiF20 at 200 KeV), and energy dispersive spectroscopy (EDS) mapping, respectively. Furthermore, the chemical state of the ions in the sample was examined by XPS (ThermoVG Scientific Instrument), using Al Kα as the X-ray source. The surface area and pore size distribution of the sample were measured by Brunauer Emmett Teller (BET) using nitrogen adsorption/desorption isotherm (Micromeritics Instrument Corp. Gemini-V).

2.3. Electrochemical Measurements

To scrutinize the electrochemical performances, the working electrode was fabricated by mixing the active materials, Ketjan black and teflonated acetylene black. The obtained paste was coated onto a stainless-steel mesh, which was then dried under vacuum at 120 °C, followed by cold pressing using a hydraulic press machine. The 2032-type coin cells were assembled in an open-air environment using glass fiber soaked with 2M $ZnSO_4$ solution as the electrolyte between the as-prepared cathode and zinc-foil anode. The electrochemical measurements were performed using WBCS 3000 (WonATech). A cyclic voltammetry (CV) test was carried out using an AUTOLAB PGSTAT302N potentiostat between 0.8 V to 1.9 V vs. Zn/Zn^{2+} at different scan rates.

3. Results and Discussion

3.1. Structural Identification and Morphological Studies

Figure 1 depicts the Rietveld refinement of calcined δ-MnO_2 using a monoclinic structure with the C2/m space group. The unit cell parameters were found to be a = 5.14, b = 2.84, and c = 7.14 Å with α = γ = 90°, β = 100.76°. The refinement was carried out using the general structure analysis system (GSAS)—II programs of Robert B. Von Dreele and Brian H. Toby [33]. The refinement parameters consisted of the scale factor and 36 background terms in a linear interpolation function and unit cell dimensions. Peak fitting, including symmetric corrections and micro-strain anisotropic broadening terms, were considered while carrying out the refinement. It is evident that all the reflections were very well accounted for during the fitting, indicating the formation of pure δ-MnO_2 with the perfect match between the observed and calculated profile. The crystal structure is also provided in the inset of Figure 1.

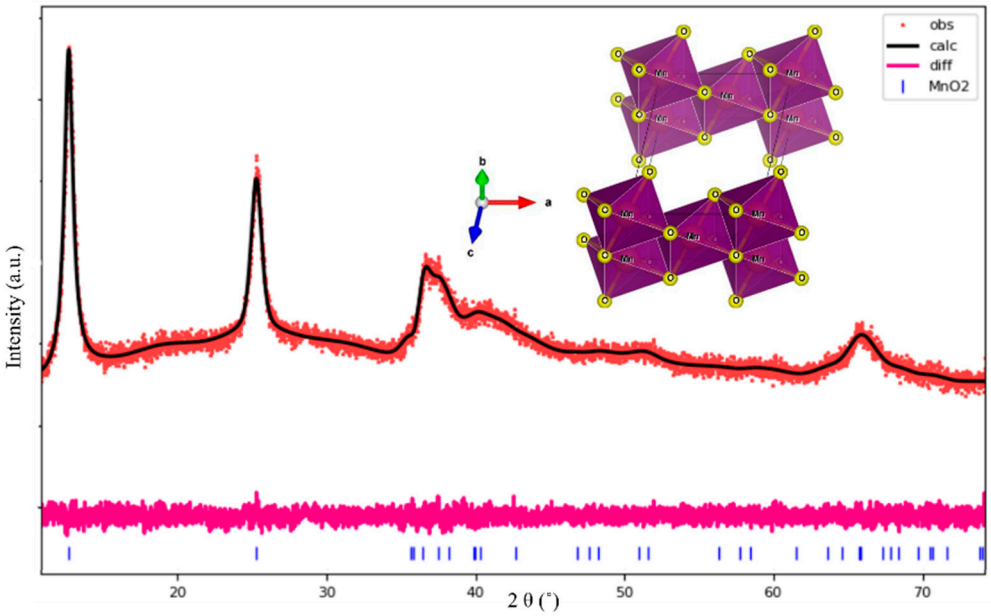

Figure 1. Rietveld refinement fit of δ-MnO_2 obtained after using monoclinic structure in the C2/m space group in the 2θ range of 10 to 75°. The red dots, black line, and pink line represents observed, calculated, and difference profiles, respectively. The vertical blue tick marks below the difference profile denotes the position of Bragg reflections.

FT-IR and Raman spectroscopy are also carried out to further confirm the crystal structure and bonding of δ-MnO_2. As shown in Figure 2a, the broad and weak absorption bands located at ~3334 cm^{-1} and ~1620 cm^{-1} represent the stretching and bending frequency of the O-H group of the interlayered water molecules, respectively [27,34]. Furthermore, the absorption bands detected around ~1110 and ~1043 cm^{-1} can be ascribed to the O-H bending vibration combined with the Mn atom [34]. On the other hand, the absorption peak found at ~468 cm^{-1} is the distinctive peak of birnessite MnO_2, as it represents the Mn-O stretching mode of the octahedral layers of the layered MnO_2 structure [27,34,35]. Raman spectroscopy was carried out between 200–1500 cm^{-1} to further confirm the structure of δ-MnO_2, as shown in Figure 2b. The three typical Raman bands can be clearly observed at ~478, ~561, and ~635 cm^{-1}, which are, in fact, the vibrational bands of δ-MnO_2. More precisely, the absorption peak obtained at ~635 cm^{-1} mainly corresponds to the symmetric stretching vibration of [MnO_6] octahedron, whereas the peaks that appeared at ~478 and ~561 cm^{-1} referred to the stretching vibration of Mn-O in the basal plane of MnO_2 sheets [14,36].

XPS is further employed to emphasize the surface chemistry and oxidation state of the ions of the fabricated δ-MnO_2 sample. Figure 3a shows the survey spectrum with a clear display of the elemental signal of only Mn, O, and C, confirming again the high purity of the sample. Furthermore, the high-resolution Mn 2p spectra shown in Figure 3b exhibits two peaks positioned at ~653.2 eV and ~641.3 eV with the splitting energy difference of ~11.8 eV between the two-spin doublet, indicating the +4 oxidation state of Mn in δ-MnO_2 [25,37]. Figure 3c shows the high-resolution XPS spectra of O 1s with the two deconvoluted peaks at ~529.2 eV and ~531.1 eV, which mainly belong to the tetravalent Mn-O-Mn bond and hydrated trivalent Mn-OH bond, respectively [25,38].

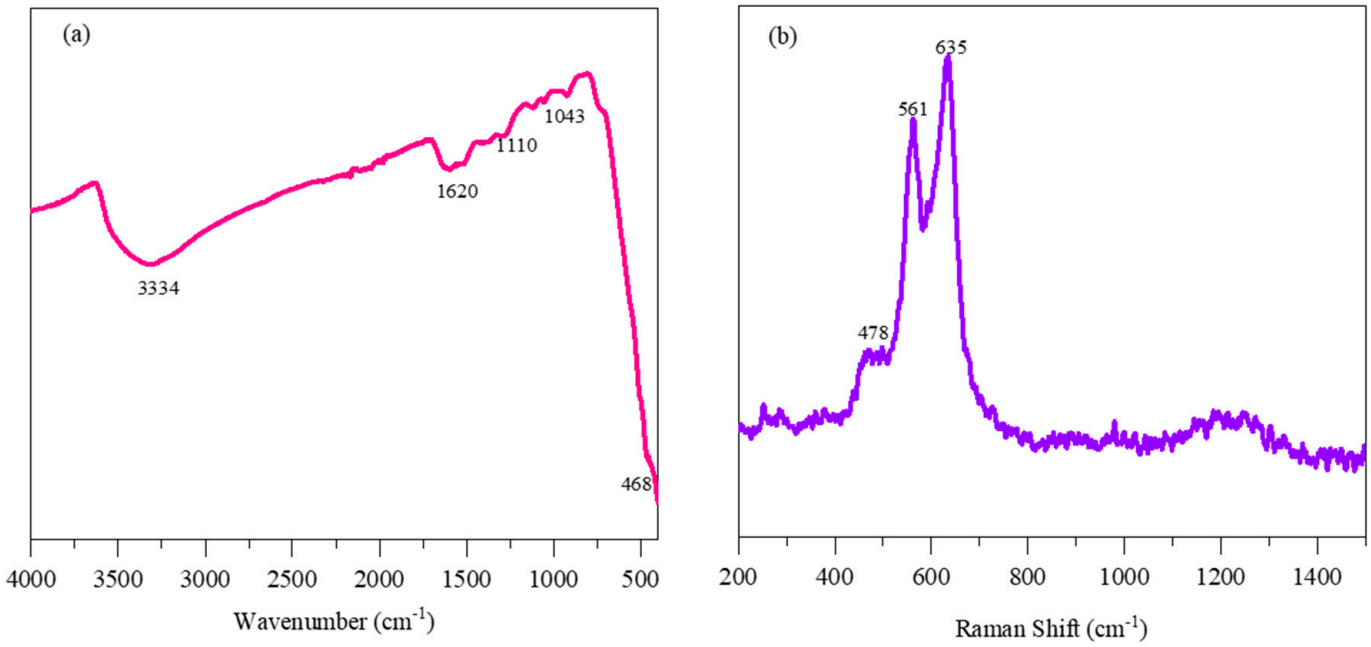

Figure 2. (**a**) Infra-red (IR) spectra; (**b**) Raman spectra of the calcined δ-MnO_2 sample.

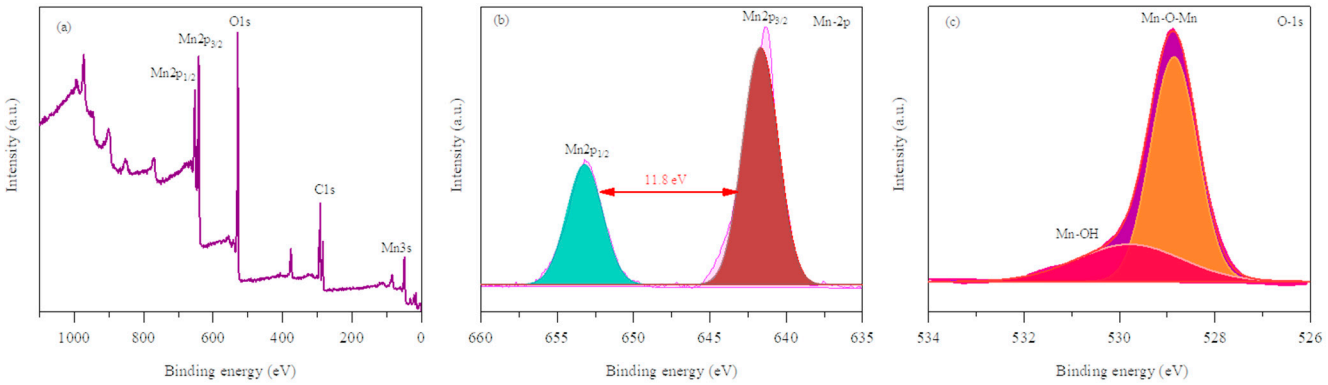

Figure 3. XPS: (**a**) survey spectrum; (**b**) Mn-2p spectra; (**c**) O-1s spectrum of δ-MnO_2 sample.

The surface morphology and detailed microstructural analysis of the calcined δ-MnO_2 sample are further characterized by FE-SEM and FE-TEM analysis. The FE-SEM image demonstrates pom-pom flower-like morphology with a diameter of nearly ~1 µm, as shown in Figure 4a. The inset of Figure 4a shows the original pom-pom flower image, as collected from Google, indicating a clear match with our current morphology. It is believed that the obtained morphology is mainly composed of primary nanosheets, which are assembled to form a pom-pom shaped flower like morphology, thereby reducing the total surface energy [25]. As can also be seen, the pom-pom flower-like morphology consists of micropores, which may provide a large contact area between the electrolyte and cathode, resulting in the fast-ion transfer during the charge/discharge processes [39]. The detailed morphological analysis is further illuminated by TEM images, as shown in Figure 4b,c, which are taken at low and high magnifications, respectively. FE-TEM images are perfectly analogous to the FE-SEM observation, demonstrating the pom-pom flower-like morphology of the calcined δ-MnO_2 sample. It is evident that the pom-pom shaped flower-like morphology is composed by the assembly of nanosheets, thus leading to the porous architecture. Moreover, the HR-TEM image (Figure 4d) exhibits a clear lattice fringe with a spacing of 0.342 nm, which corresponds to the (002) plane of δ-MnO_2. Energy dispersive spectra (EDS) were also employed to confirm the pure phase formation of calcined δ-MnO_2.

The elemental mapping affirms the presence of a homogenous distribution of Mn (Mn-K: red) and O (O-K: green) without the presence of any other impurities, as shown in Figure 4e,f, respectively.

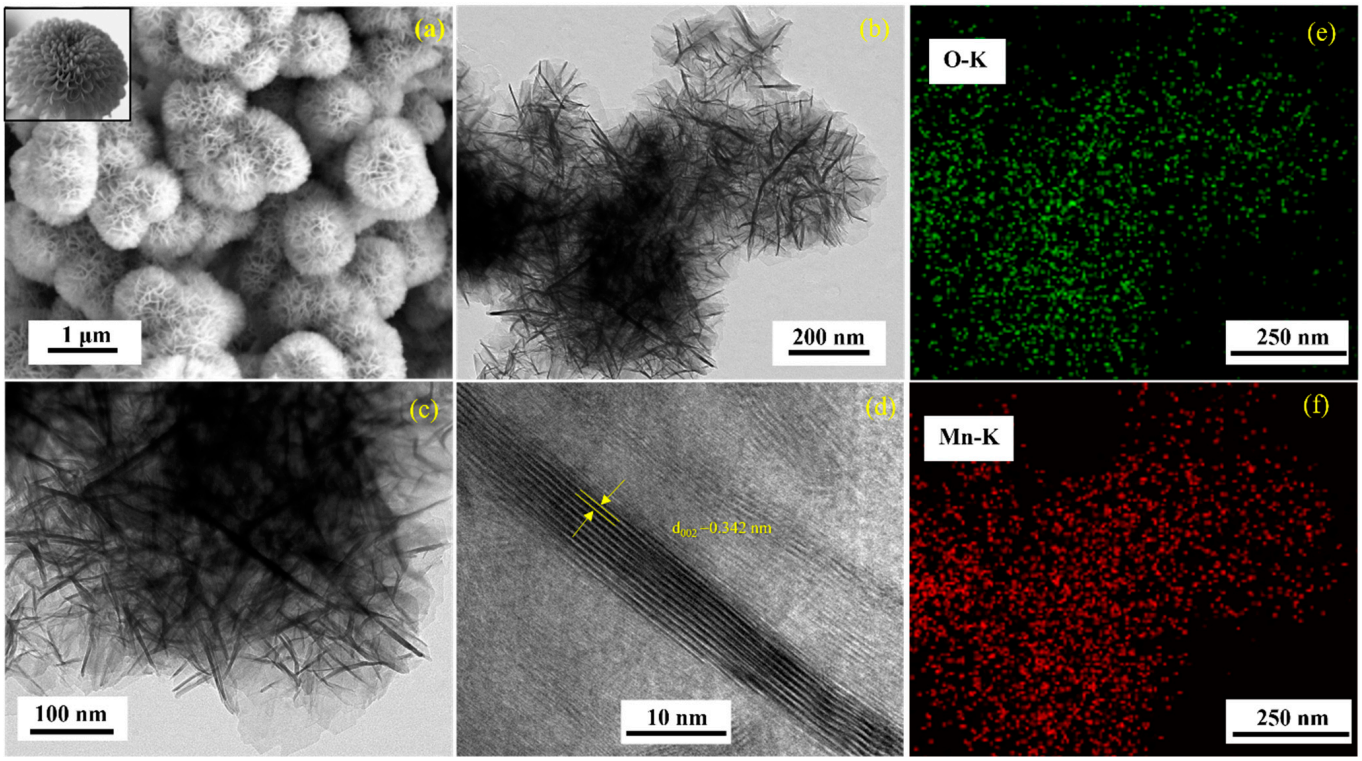

Figure 4. Morphological characterizations: (**a**) FE-SEM image; (**b**,**c**) FE-TEM images at different magnifications; (**d**) HR-TEM image; (**e**,**f**) representative EDX mapping images of δ-MnO_2 sample.

The specific surface area and pore-size distribution of the pom-pom flower-like morphology of δ-MnO_2 were further investigated by the Brunauer-Emmett-Tellar (BET) measurement, using a nitrogen adsorption/desorption isotherm. Figure 5 displays a type IV isotherm with an H3 hysteresis loop, illustrating the existence of mesoporosity in the sample. The inset of Figure 5 shows a Barrett-Joyner-Halenda (BJH) adsorption pore-size distribution curve with an average pore diameter of ~9.8 nm and a total pore volume of ~0.0585 cm^3g^{-1}. The specific surface area of the δ-MnO_2 sample is found to be ~21.085 m^2g^{-1}. The existence of a porous morphology within a pom-pom shape flower-like morphology of δ-MnO_2 offers high surface area along with a reduced diffusion distance for Zn^{2+} ions, which eventually improved the overall conductivity of the cathode and enhanced the electrochemical performances. It is also believed that the porosity reduces the risk of mechanical degradation and improves the overall lifespan of the battery [40,41].

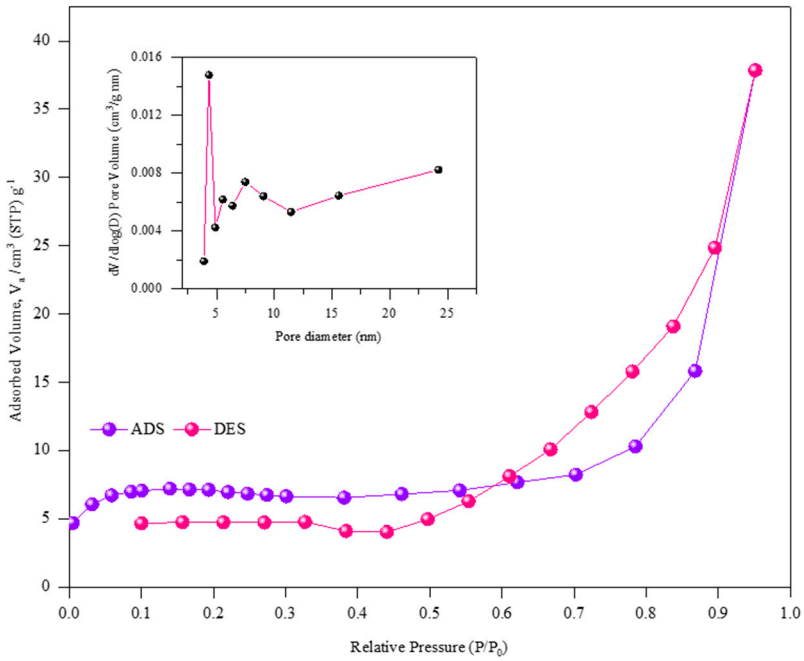

Figure 5. N_2 adsorption/desorption isotherm and BJH pore-size distribution (inset) curve of the calcined δ-MnO_2 sample.

3.2. Electrochemical Performances

Since δ-MnO_2 acts as an excellent host for zinc-ion insertion due to its layered structure, it gives better electrochemical results. As represented in Figure 6a, the electrochemical performance of pom-pom shaped flowerlike δ-MnO_2 was first determined by cyclic voltammetry (CV) at varied scan rates ranging from 0.1 mV s^{-1} to 2 mV s^{-1}, which exhibits similar characteristics. The two cathodic peaks were observed at ~1.2 V and ~1.3 V, which can be ascribed to the intercalation of Zn^{2+} and H^+ ions into MnO_2 and the reduction of Mn^{4+} into its lower oxidation state, respectively. In contrast, the two anodic peaks located at ~1.5 V and ~1.6 V are due to the de-intercalation of Zn^{2+} and H^+ ions from MnO_2 and the oxidation of Mn^{3+} to Mn^{4+}, respectively [37]. Thus, it can be concluded that it is a two-step reaction of Zn^{2+} ion insertion followed by the formation of spinel-type $ZnMn_2O_4$ [37]. The detailed reaction mechanism is discussed in the later sections. The peak shifting can be clearly noticed with the increase in the scan rates, which indicates the high reversibility and excellent cycling stability during the polarization period [37]. The capacitive current is also quantitively calculated using CV data at different scan rates by applying the following equation:

$$i = av^b \quad (1)$$

where i is the peak-specific current, v is the scan rate, and a and b are constants. Equation (1) can be expressed in the logarithm form as shown in Equation (2):

$$\log i = b \log v + \log a \quad (2)$$

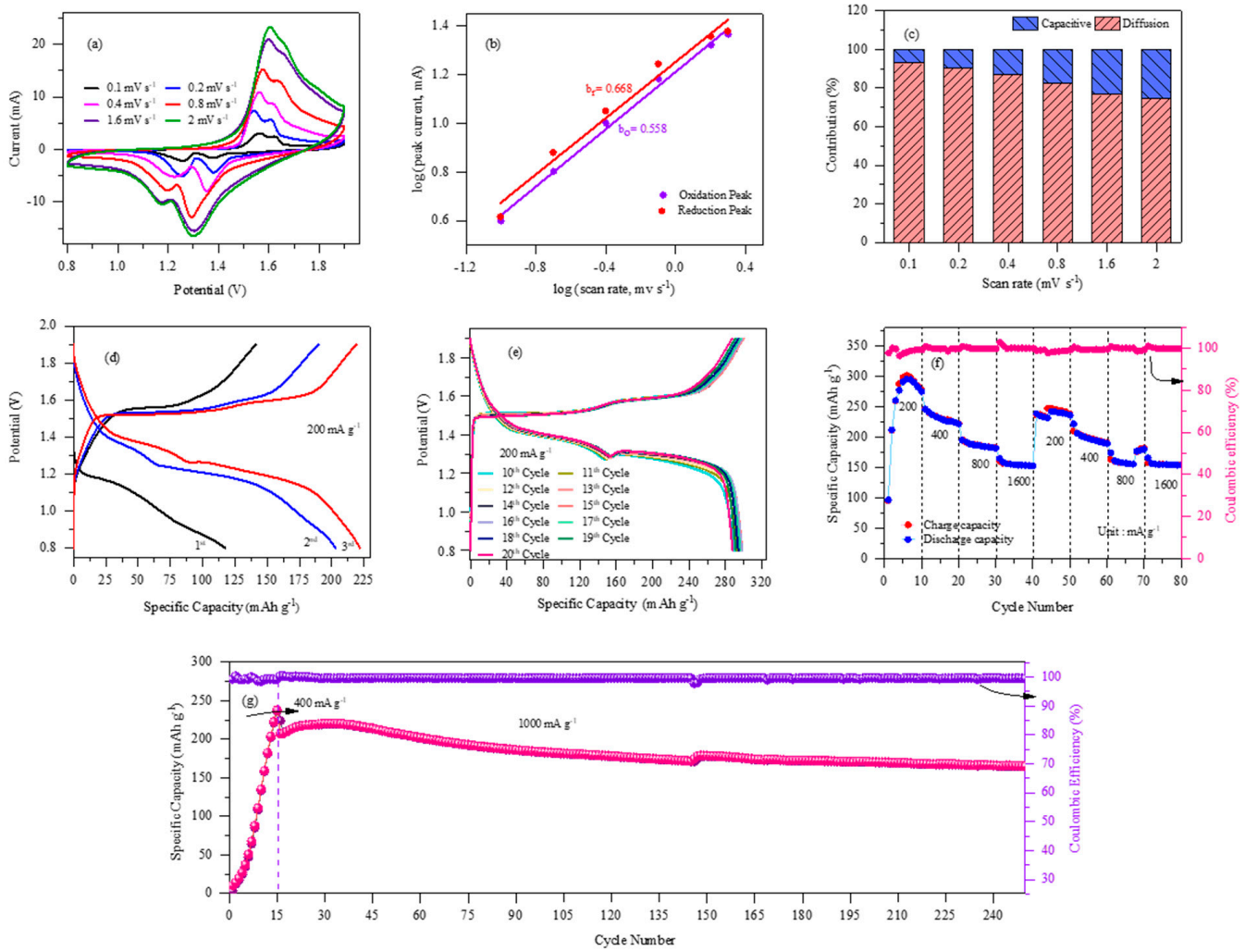

Figure 6. Electrochemical performances of δ-MnO_2 sample: (**a**) cyclic voltammetry curves at different current densities; (**b**) linear relationship between the logarithm of peak current and scan rates; (**c**) corresponding capacitive and diffusion contribution ratio to the total capacity of δ-MnO_2 sample; (**d**,**e**) galvanostatic discharge/charge curves at a constant current density of 200 mA g^{-1} for initial three cycles and then, successive 20 cycles, respectively; (**f**) C-rate performances at various current densities; (**g**) long-term cycling performance at 1000 mA g^{-1}.

It is found that the material shows supercapacitor and battery behavior if the value of b is close to 1 and 0.5, respectively. The value of b can be calculated by plotting a linear graph between log i and log v, where b is the slope of the graph, as displayed in Figure 6b. Since the graph clearly shows a good linear relationship, it indicates the diffusion-controlled characteristic during the charge storage process [37]. The calculated value of b for the anodic and cathodic processes are ~0.558 and ~0.668, respectively. Since the average value of b is nearly 0.613, which is close to 0.5, it determines the diffusion-controlled mechanism (battery behavior) for the δ-MnO_2 cathode. Furthermore, the diffusion/surface-confined contribution can be evaluated using the following equations:

$$\begin{array}{c} i(V) = k_1 v + k_2 v^{1/2} \text{ or} \\ \frac{i(V)}{v^{\frac{1}{2}}} = k_1 v^{1/2} + k_2 \end{array} \quad (3)$$

where $i(V)$ is the total current at a constant potential; and $k_1 v$ and $k_2 v^{1/2}$ represent the separate contribution of surface capacitive effects and diffusion-controlled insertion, respectively. The value of k_1 and k_2 can be obtained from the slope and intercept of a linear

plot of $i(V)/v^{1/2}$ versus $v^{1/2}$. Though the current contribution from the surface capacitive effect (k_1v) and diffusion-controlled insertion processes ($k_2v^{1/2}$) are also calculated, the diffusion-controlled contribution is near ~90% at 0.1 mV s^{-1}, as shown in the bar graph of Figure 6c. However, this ratio keeps decreasing as the scan rate increases and eventually reaches the final value of ~70% for the diffusion-controlled mechanism at 2 mV s^{-1}. Thus, it can be suggested that this process takes less time for electrolyte ions to diffuse and react with internal active materials [37]. Figure 6d and e represent the galvanostatic charge/discharge curves of the pom-pom shape flower-like mesoporous δ-MnO_2 cathode at a constant current density of 200 mA g^{-1} within the voltage window of 0.8 V to 1.9 V for the initial 3 cycles and 10th to 20th cycles, respectively. Upon the first discharge, the potential of the cell sharply decreases until 0.8 V vs. Zn^{2+}/Zn with a specific capacity of ~120 mAh g^{-1}, while on the subsequent charge, the potential of the cell smoothly increases up to 1.9 V with the clear plateau at 1.6 V and specific capacity of ~141 mAh g^{-1}. Furthermore, the discharge/charge capacity for the 2nd and 3rd cycles is found to be ~202/189 mAh g^{-1} and ~220/221 mAh g^{-1}, respectively, with a significant enhancement of ~100% into the coulombic efficiency. More importantly, it can be also observed from Figure 6e that the pom-pom shape flower-like δ-MnO_2 exhibits high reversibility in the successive cycles with nearly the same discharge/charge capacity at constant discharge and charge potential plateaus at 1.3 V and 1.5 V, respectively. The electrode delivered the specific capacity of ~299.9/298.9 mAh g^{-1} for the 20th cycle with almost 100% coulombic efficiency. Since the layered δ-MnO_2 host has a large interlayer distance including this novel porous morphology, it is believed that the insertion/de-insertion of Zn^{2+} ions is highly favorable and accelerated; and thus, a decent capacity is achieved. More importantly, the plateaus are in accordance with the CV results [24,38]. The significant difference observed between the first and successive discharge and charge cycles can be accredited to the inappropriate wetting of the electrode and the gradual activation of the electrode material [27]. In addition, the electrode's high surface area along with the mesoporosity may also help to accommodate the absolute volume expansion/contraction that occurred during the charge and discharge of Zn^{2+} ions. Moreover, Figure 6e exhibits the perfect overlapping between the discharge and charge cycles with nearly similar capacity after the initial three cycles, indicating the excellent reversibility of the electrode material.

To further examine the rate capability, the pom-pom flower-like δ-MnO_2 electrode was cycled at various current densities ranging between 200 mA g^{-1} to 1600 mA g^{-1}, as displayed in Figure 6f. Upon cycling for 10 cycles at each of the current densities of 200, 400, 800, and 1600 mA g^{-1}, the electrode material delivered charge capacities of ~290.9, ~230.5, ~186.4, and ~154.3 mAh g^{-1}, respectively. The decrease in capacity with the increase of current density is a general phenomenon, as ions do not attain sufficient time to insert/de-insert at high current rates. However, it is worth noticing that the capacity fading at a high current density is considerably less as compared to the increment in the current density from 400 to 1600 mA g^{-1}. Therefore, the obtained high-rate performances can be attributed to the current unique morphology with mesoporosity, which may have offered more active sites for electrochemical reactions and numerous diffusion channels for Zn^{2+} insertion/de-insertions [40]. Furthermore, when the current density again returned to all the current densities, the recovery of the specific capacity was near ~82%, indicating the high structural stability of the pom-pom flower-like δ-MnO_2 electrode.

To further evaluate the structural stability of the pom-pom flower-like δ-MnO_2 electrode, the cycling performance was tested again at 400 mA g^{-1} for the initial 15 cycles, followed by 1000 mA g^{-1} until 250 cycles, as shown in Figure 6g. After the activation of the electrode at 400 mA g^{-1}, the electrode shows stable and distinguished cycling performances at a high current density of 1000 mA g^{-1}, without any significant capacity decay until 250 cycles. The specific capacity is found to be ~238 mAh g^{-1} for the 15th cycle at 400 mA g^{-1}, which remained ~166 mAh g^{-1} after 250 cycles with nearly 100% coulombic efficiency, again indicating the high durability of the electrode material. As per the comparative Table 1, which includes various morphologies, and their corresponding discharge

capacity with the number of cycles and current densities of the reported δ-MnO_2 electrode, the obtained pom-pom flower-like δ-MnO_2 electrode in the present work delivered superior electrochemical performances among all the reported data.

Table 1. A comparison between the specific capacities of the current pom-pom flower-like morphology of δ-MnO_2 electrode and previously reported δ-MnO_2 electrode based on various morphologies.

Material	Morphology	Specific Capacity/Cycle Number/Current Densities	Ref.
δ-MnO_2	Nanosheets	133 mAh g^{-1} after 100 cycles at 100 mAg^{-1}	[27]
δ-MnO_2/graphite	Nanoflower	114 mAh g^{-1} after 100 cycles at 400 mAg^{-1}	[39]
δ-MnO_2	Submicrospheres	96 mAh g^{-1} after 100 cycles at 100 mAg^{-1}	[14]
Ni doped δ-MnO_2	Random particles	16t mAh g^{-1} after 110 cycles at 100 mAg^{-1}	[42]
δ-MnO_2	Floret-like particles	60 mAh g^{-1} after 125 cycles at C/25 C-rate	[13]
δ-MnO_2	Flower-like	70 mAh g^{-1} after 100 cycles at 100 mAg^{-1}	[43]
δ-MnO_2	Flake-like particles	97 mAh g^{-1} after 50 cycles at 100 mAg^{-1}	[44]
δ-MnO_2/CNT	Flower-like	96 mAh g^{-1} after 100 cycles at 400 mAg^{-1}	[45]
KMO-NNT *	Nanowire	148 mAh g^{-1} after 400 cycles at 1.623C	[46]
δ-MnO_2	Nanoflake	112 mAh g^{-1} after 100 cycles at 83 mAg^{-1}	[47]
δ-MnO_2	Flower-like	80 mAh g^{-1} after 70 cycles at 200 mAg^{-1}	[48]
δ-MnO_2	Pom-pom shaped flower	166 mAh g^{-1} after 250 cycles at 1000 mAg^{-1}	Our work

* KMO-NNT: K^+-inserted δ-MnO_2 nanowires.

Since the different reaction mechanisms, such as H^+/Zn^{2+} insertion, conversion reaction, and deposition-dissolution reactions, have been reported so far for ZIBs, ex situ XRD was conducted after the 200th cycles to confirm the storage mechanism and structural stability of the pom-pom shape flower-like δ-MnO_2 electrode; and the obtained result is shown in Figure 7. As can be seen, the diffraction peaks that appeared at ~25.7° and ~34.2° mainly belong to MnOOH (JCPDS No. 41-1379), demonstrating the intercalation of H^+. On the other hand, the reflections located at ~36.9°, ~59.8°, and ~68.6° can be well indexed with the spinel $ZnMn_2O_4$ (JCPDS No. 24-1133), which also confirmed the insertion of Zn^{2+}. Furthermore, since the H^+ ion becomes consumed during the discharge, it indicates the formation of MnOOH, which increases the concentration of OH^- in the electrolyte around electrode surfaces [25]. Therefore, the existence of OH^- tends to participate in the formation of $Zn_4SO_4(OH)_6.5H_2O$, which is also found in the ex-situ XRD pattern. Hence, it is believed that the following reactions take place at the cathode and anode:

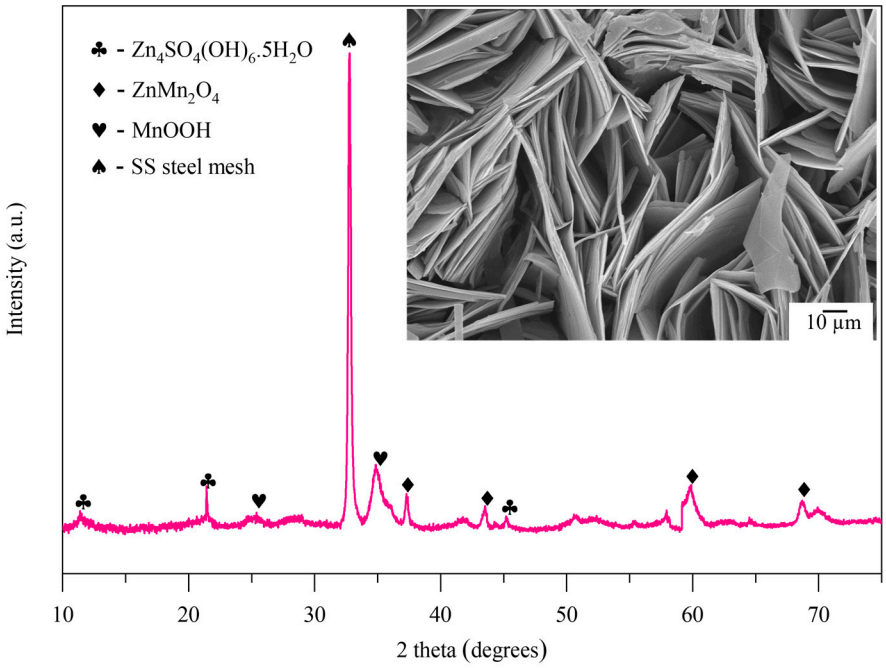

Figure 7. Ex situ X-ray diffraction pattern and ex situ SEM (inset) of the δ-MnO_2 electrode after 200 cycles.

Cathode:

$$MnO_2 + H^+ + e^- \rightarrow MnOOH \quad (4)$$

$$2MnO_2 + Zn^{2+} + 2e^- \rightarrow ZnMn_2O_4 \quad (5)$$

$$4Zn^{2+} + SO_4^{2-} + 6OH^- + 2e^- + 5H_2O \rightarrow Zn_4SO_4(OH)_6.5H_2O \quad (6)$$

Anode:

$$Zn \rightarrow Zn^{2+} + 2e^- \quad (7)$$

Thus, both H^+ and Zn^{2+} ions intercalate into the layered δ-MnO_2 during discharge and act as a support pillar to the layered structure, followed by the deposition of $Zn_4SO_4(OH)_6 \cdot 5H_2O$ (ZSH). To confirm the formation of ZSH, ex situ SEM was also carried out after 200 cycles in the discharged state, which is given in the inset of Figure 7. The obtained image is almost like the reported ZSH data, which further approves the H^+ and Zn^{2+} intercalation mechanism and the existence of ZSH in the δ-MnO_2 sample [25]. Based on the above observation, it can be concluded that the layered structure is gradually transformed into a spinel phase upon long-range cycling. Hence, the obtained pom-pom flower-like morphology of the δ-MnO_2 electrode provides a high reversible capacity and excellent cycling stability under the abovementioned reaction mechanisms.

4. Conclusions

In summary, a novel pom-pom flower-like mesoporous δ-MnO_2 cathode was successfully synthesized using a hydrothermal synthesis method, followed by annealing at 360 °C for 2 h under air atmosphere. The mesoporous nature shortened the diffusion distance of Zn^{2+} ions along with accommodation of the volume changes that occurred during Zn^{2+} ions insertion/de-insertion, and thereby, offered better electrochemical results. Since the obtained δ-MnO_2 electrode delivered a specific capacity of ~166 mAh g^{-1} after 250 cycles at a high current density of 1000 mAg^{-1}, it indicates the high suitability of the δ-MnO_2 cathode for aqueous zinc-ion batteries. Furthermore, the ex-situ study confirmed the two-step insertion of H^+ and Zn^{2+} ions accompanied by the precipitation/dissolution of $Zn_4SO_4(OH)_6 \cdot 5H_2O$ (ZSH) into a pom-pom shape flower-like δ-MnO_2 cathode during discharge/charge processes. It is believed that the present work offers a novel synthesis

route to achieve a δ-MnO_2 cathode for the high capacity and long lifespan of zinc-ion batteries.

Author Contributions: Conceptualization, P.Y. and A.K.R.; methodology, P.Y.; software, D.P. and J.K.; validation, A.K.R. and J.K.; formal analysis, A.K.R.; investigation, P.Y.; resources, P.Y.; data curation, D.P.; writing—original draft preparation, P.Y.; writing—review and editing, A.K.R.; visualization, D.P.; supervision, A.K.R.; project administration, A.K.R.; funding acquisition, A.K.R. and J.K. All authors have read and agreed to the published version of the manuscript.

Funding: This work was mainly funded by the Council of Scientific and Industrial Research (CSIR) Research Grant (File No. 01(3015)/21/EMR-II) and partially supported by the National Research Foundation of Korea (NRF) grant funded by the Korean government (MSIT) (NRF-2018R1A5A1025224).

Acknowledgments: P.Y. would like to thank CSIR, New Delhi, for the award of junior research fellowship. A.K.R. is grateful to the University Grants Commission (UGC) for the position under the UGC-FRP scheme (FRP ID: 57304). The author would also like to extend heartfelt thanks to the University Science Instrumentation Centre (USIC) for sample characterizations.

Conflicts of Interest: The authors declare no conflict of interest.

References

1. Islam, S.; Alfaruqi, M.H.; Mathew, V.; Song, J.; Kim, S.; Kim, S.; Jo, J.; Baboo, J.P.; Pham, D.T.; Putro, D.Y.; et al. Facile synthesis and the exploration of the zinc storage mechanism of β-MnO_2 nanorods with exposed (101) planes as a novel cathode material for high performance eco-friendly zinc-ion batteries. *J. Mater. Chem. A* **2017**, *5*, 23299. [CrossRef]
2. Li, W.; Dahn, J.R.; Wainwright, D.S. Rechargeable Lithium Batteries with Aqueous Electrolytes. *Science* **1994**, *264*, 1115–1118. [CrossRef] [PubMed]
3. Wang, R.Y.; Wessells, C.D.; Huggins, R.A.; Cui, Y. Highly Reversible Open Framework Nanoscale Electrodes for Divalent Ion Batteries. *Nano Lett.* **2013**, *13*, 5748–5752. [CrossRef]
4. Alfaruqi, M.H.; Gim, J.; Kim, S.; Song, J.; Jo, J.; Kim, S.; Mathew, V.; Kim, J. Enhanced reversible divalent zinc storage in a structurally stable α-MnO_2 nanorod electrode. *J. Power Sources* **2015**, *288*, 320–327. [CrossRef]
5. Leisegang, T.; Meutzner, F.; Zschornak, M.; Münchgesang, W.; Schmid, R.; Nestler, T.; Eremin, R.A.; Kabanov, A.A.; Blatov, V.A.; Meyer, D.C. The aluminum-ion battery: A sustainable and seminal concept? *Front. Chem.* **2019**, *7*, 268. [CrossRef]
6. Mokhtar, M.; Talib, M.Z.M.; Majlan, E.H.; Tasirin, S.M.; Ramli, W.M.F.W.; Daud, W.R.W.; Sahari, J. Recent developments in materials for aluminum-air batteries: A review. *J. Ind. Eng. Chem.* **2015**, *32*, 1–20. [CrossRef]
7. Lao-atiman, W.; Julaphatachote, T.; Boonmongkolras, P.; Kheawhom, S. Printed transparent thin film Zn-Mn_2 battery. *J. Electrochem. Soc.* **2017**, *164*, A859–A863. [CrossRef]
8. De Juan-Corpuz, L.M.; Corpuz, R.D.; Somwangthanaroj, A.; Nguyen, M.T.; Yonezawa, T.; Ma, J.; Kheawhom, S. Binder-free centimeter-long V_2O_5 nanofibers on carbon cloth as cathode material for Zinc-Ion batteries. *Energies* **2019**, *13*, 31. [CrossRef]
9. Hosseini, S.; Abbasi, A.; Uginet, L.O.; Haustraete, N.; Praserthdam, S.; Yonezawa, T.; Kheawhom, S. The influence of dimethyl sulfoxide as electrolyte additive on anodic dissolution of alkaline Zinc-Air Flow Battery. *Sci. Rep.* **2019**, *9*, 14958. [CrossRef]
10. Ling, C.; Zhang, R. Manganese dioxide as rechargeable magnesium battery cathode. *Front. Energy Res.* **2017**, *5*, 30. [CrossRef]
11. Shrestha, N.; Raja, K.S.; Utgikar, V. Mg-RE alloy anode materials for Mg-Air battery application. *J. Electrochem. Soc.* **2019**, *166*, A3139–A3153. [CrossRef]
12. Tian, H.; Gao, T.; Li, X.; Wang, X.; Luo, C.; Fan, X.; Yang, C.; Suo, L.; Ma, Z.; Han, W.; et al. High power rechargeable magnesium/iodine battery chemistry. *Nat. Commun.* **2017**, *8*, 14083. [CrossRef]
13. Han, S.D.; Kim, S.; Li, D.; Petkov, V.; Yoo, H.D.; Phillips, P.J.; Wang, H.; Kim, J.J.; More, K.L.; Key, B.; et al. Mechanism of Zn Insertion into Nanostructured δ-MnO_2: A Nonaqueous Rechargeable Zn Metal Battery. *Chem. Mater.* **2017**, *29*, 4874–4884. [CrossRef]
14. Guo, C.; Zhou, Q.; Liu, H.; Tian, S.; Chen, B.; Zhao, J.; Li, J. A case study of β- and δ-MnO_2 with different crystallographic forms on ion-storage in rechargeable aqueous zinc ion battery. *Electrochim. Acta* **2019**, *324*, 134867. [CrossRef]
15. Wang, L.; Zheng, J. Recent advances in cathode materials of rechargeable aqueous zinc ion batteries. *Mater. Today Adv.* **2020**, *7*, 100078. [CrossRef]
16. Corpuz, R.D.; Juan-Corpuz, L.M.D.; Nguyen, M.T.; Yonezawa, T.; Wu, H.L.; Somwangthanaroj, A.; Kheawhom, S. Binder-Free α-MnO_2 Nanowires on Carbon Cloth as Cathode Material for Zinc-Ion Batteries. *Int. J. Mol. Sci.* **2020**, *21*, 3113. [CrossRef]
17. Kundu, D.; Adams, B.D.; Duffort, V.; Vajargah, S.H.; Nazar, L.F. A high-capacity and long-life aqueous rechargeable zinc battery using a metal oxide intercalation cathode. *Nat. Energy* **2016**, *1*, 16119. [CrossRef]
18. Liu, Z.; Pulletikurthi, G.; Endres, F. A Prussian Blue/Zinc Secondary Battery with a Bio-Ionic Liquid-Water Mixture as Electrolyte. *ACS Appl. Mater. Interfaces* **2016**, *8*, 12158–12164. [CrossRef]
19. Zhang, L.; Chen, L.; Zhou, X.; Liu, Z. Towards High-Voltage Aqueous Metal-Ion Batteries Beyond 1.5 V: The Zinc/Zinc Hexacyanoferrate System. *Adv. Energy Mater.* **2015**, *5*, 1400930. [CrossRef]

20. Li, W.; Wang, K.; Cheng, S.; Jiang, K. A long-life aqueous Zn-ion battery based on $Na_3V_2(PO_4)_2F_3$ cathode. *Energy Storage Mater.* **2018**, *15*, 14–21. [CrossRef]
21. Liu, W.; Zhang, X.; Huang, Y.; Jiang, B.; Chang, Z.; Xu, C.; Kang, F. β-MnO_2 with proton conversion mechanism in rechargeable zinc ion battery. *J. Energy Chem.* **2021**, *56*, 365–373. [CrossRef]
22. Yadav, P.; Kumari, N.; Rai, A.K. A review on solutions to overcome the structural transformation of manganese dioxide-based cathodes for aqueous rechargeable zinc ion batteries. *J. Power Sources* **2023**, *555*, 232385. [CrossRef]
23. Trcoli, R.; Mantia, L. An Aqueous Zinc-Ion Battery Based on Copper Hexacyanoferrate. *ChemSusChem* **2015**, *8*, 481–485. [CrossRef] [PubMed]
24. Ming, F.; Liang, H.; Lei, Y.; Kandambeth, S.; Eddaoudi, M.; Alshareef, H.N. Layered $Mg_xV_2O_5{\cdot}nH_2O$ as Cathode Material for High-Performance Aqueous Zinc Ion Batteries. *ACS Energy Lett.* **2018**, *3*, 2602–2609. [CrossRef]
25. Liu, P.; Wang, M.; Li, J.; Cui, H.; Zeng, T.; Yang, S.; Wang, H.; Liu, Y. Microwave-induced structural tunability of 3D δ-MnO_2 microflowers for high-performance aqueous Zn-ion batteries. *Ceram. Int.* **2021**, *47*, 25558–25566. [CrossRef]
26. Huang, A.; Zhou, W.; Wang, A.; Chen, M.; Tian, Q.; Chen, J. Molten salt synthesis of α-MnO_2/Mn_2O_3 nanocomposite as a high-performance cathode material for aqueous zinc-ion batteries. *J. Energy Chem.* **2021**, *54*, 475–481. [CrossRef]
27. Guo, C.; Liu, H.; Li, J.; Hou, Z.; Liang, J.; Zhou, J.; Zhu, Y.; Qian, Y. Ultrathin δ-MnO_2 nanosheets as cathode for aqueous rechargeable zinc ion battery. *Electrochim. Acta* **2019**, *304*, 370–377. [CrossRef]
28. Zhang, Y.; Liu, Y.; Liu, Z.; Wu, X.; Wen, Y.; Chen, H.; Ni, X.; Li, G.; Huang, J.; Peng, S. MnO_2 cathode materials with the improved stability via nitrogen doping for aqueous zinc-ion batteries. *J. Energy Chem.* **2022**, *64*, 23–32. [CrossRef]
29. Cao, J.; Zhang, D.; Zhang, X.; Wang, S.; Han, J.; Zhao, Y.; Huang, Y.; Qin, J. Mechanochemical reactions of MnO_2 and graphite nanosheets as a durable zinc ion battery cathode. *Appl. Surf. Sci.* **2020**, *534*, 1476. [CrossRef]
30. Zhang, N.; Cheng, F.; Liu, J.; Wang, L.; Long, X.; Liu, X.; Li, F.; Chen, J. Rechargeable aqueous zinc-manganese dioxide batteries with high energy and power densities. *Nat. Commun.* **2017**, *8*, 405. [CrossRef] [PubMed]
31. Lee, B.; Lee, H.R.; Kim, H.; Chung, K.Y.; Cho, B.W.; Oh, S.H. Elucidating the intercalation mechanism of zinc ions into alpha-MnO_2 for rechargeable zinc batteries. *Chem. Commun.* **2015**, *51*, 9265–9268. [CrossRef]
32. Xia, A.; Yu, W.R.; Yi, J.; Tan, G.; Ren, H.; Liu, C. Synthesis of porous δ-MnO_2 nanosheets and their supercapacitor performance. *J. Electroanal. Chem.* **2019**, *839*, 25–31. [CrossRef]
33. Toby, B.H.; Von Dreele, R.B. GSAS-II: The genesis of a modern open-source all-purpose crystallography software package. *J. Appl. Cryst.* **2013**, *46*, 544–549. [CrossRef]
34. Huang, M.; Zhang, Y.; Li, F.; Zhang, L.; Ruoff, R.S.; Wen, Z.; Liu, Q. Self-Assembly of Mesoporous Nanotubes Assembled from Interwoven Ultrathin Birnessite-type MnO_2 Nanosheets for Asymmetric Supercapacitors. *Sci. Rep.* **2014**, *4*, 3878. [CrossRef]
35. Kang, L.; Zhang, M.; Liu, Z.H.; Ooi, K. IR spectra of manganese oxides with either layered or tunnel structures. *Spectrochim. Acta Mol. Biomol. Spectrosc.* **2007**, *67*, 864–869. [CrossRef]
36. Julien, C.; Massot, M.; Baddour-Hadjean, R.; Franger, S.; Bach, S.; Pereira- Ramos, J.P. Raman spectra of birnessite manganese dioxides. *Solid State Ion.* **2003**, *159*, 345–356. [CrossRef]
37. Wang, H.; Liang, M.; Gao, J.; Ma, C.; He, Z.; Zhao, Y.; Miao, Z. Robust structural stability of flower-like δ-MnO_2 as cathode for aqueous zinc ion battery. *Colloids Surf. A Physicochem. Eng.* **2022**, *643*, 128804. [CrossRef]
38. Wang, D.; Wang, L.; Liang, G.; Li, H.; Liu, Z.; Tang, Z.; Liang, J.; Zhi, C. A Superior δ-MnO_2 Cathode and a Self-Healing Zn-δ-MnO_2 Battery. *ACS Nano* **2019**, *13*, 10643–10652. [CrossRef]
39. Khamsanga, S.; Pornprasertsuk, R.; Yonezawa, T.; Mohamad, A.A.; Kheawhom, S. δ-MnO_2 nanoflower/graphite cathode for rechargeable aqueous zinc ion batteries. *Sci. Rep.* **2019**, *9*, 8441. [CrossRef]
40. Wang, J.; Wang, J.G.; Liu, H.; Wei, C.; Kang, F. Zinc ion stabilized MnO_2 nanospheres for high capacity and long lifespan aqueous zinc-ion batteries. *J. Mater. Chem. A* **2019**, *7*, 13727–13735. [CrossRef]
41. Huang, J.; Wang, Z.; Hou, M.; Dong, X.; Liu, Y.; Wang, Y.; Xia, Y. Polyaniline-intercalated manganese dioxide nanolayers as a high-performance cathode material for an aqueous zinc-ion battery. *Nat. Commun.* **2018**, *9*, 2906. [CrossRef]
42. Gao, D.; Zhu, T.; Yu, L.; Chen, P.; Li, C.; Liu, Y. Ni-doped δ-MnO_2 as a cathode for Zn-ion batteries. *IOP Conf. Ser. Earth Environ. Sci.* **2021**, *844*, 012007. [CrossRef]
43. Corpuz, R.D.; Juan, L.M.Z.D.; Praserthdam, S.; Pornprasertsuk, R.; Yonezawa, T.; Thanhnguyen, M.; Khawhom, S. Annealing induced a well-ordered single crystal δ-MnO_2 and its electrochemical performance in zinc-ion battery. *Sci. Rep.* **2019**, *9*, 15107. [CrossRef] [PubMed]
44. Alfaruqi, M.H.; Islam, S.; Putro, D.Y.; Mathew, V.; Kim, S.; Jo, J.; Kim, S.; Sun, Y.K.; Kim, K.; Kim, J. Structural transformation and electrochemical study of layered MnO_2 in rechargeable aqueous zinc-ion battery. *Electrochim. Acta* **2018**, *276*, 1–11. [CrossRef]
45. Liu, D.S.; Mai, Y.; Chen, S.; Liu, S.; Ang, E.H.; Ye, M.; Yang, Y.; Zhang, Y.; Geng, H.; Li, C.C. A 1D-3D interconnected δ-MnO_2 nanowires network as high-performance and high energy efficiency cathode material for aqueous zinc-ion batteries. *Electrochim. Acta* **2021**, *370*, 137740. [CrossRef]
46. Khamsanga, S.; Nguyen, M.T.; Yonezawa, T.; Thamyongkit, P.; Pornprasertsuk, R.; Pattananuwat, P.; Tuantranont, A.; Siwamogsatham, S.; Kheawhom, S. MnO_2 Heterostructure on Carbon Nanotubes as Cathode Material for Aqueous Zinc-Ion Batteries. *Int. J. Mol. Sci.* **2020**, *21*, 4689. [CrossRef]

47. Alfaruqi, M.H.; Gim, J.; Kim, S.; Song, J.; Pham, D.T.; Jo, J.; Xiu, Z.; Mathew, V.; Kim, J. A layered δ-MnO_2 nanoflake cathode with high zinc-storage capacities for eco-friendly battery applications. *Electrochem. Commun.* **2015**, *60*, 121–125. [CrossRef]
48. Zhao, Y.; Zhang, P.; Liang, J.; Xia, X.; Ren, L.; Song, L.; Liu, W.; Sun, X. Uncovering sulfur doping effect in MnO_2 nanosheets as an efficient cathode for aqueous zinc ion battery. *Energy Storage Mater.* **2022**, *47*, 424–433. [CrossRef]